

See discussions, stats, and author profiles for this publication at: <https://www.researchgate.net/publication/231652093>

# Photoelectrochemical Properties of Crystalline Perovskite Lanthanum Titanium Oxynitride Films under Visible Light

ARTICLE *in* THE JOURNAL OF PHYSICAL CHEMISTRY C · APRIL 2009

Impact Factor: 4.77 · DOI: 10.1021/jp811100r

---

CITATIONS

50

---

READS

140

8 AUTHORS, INCLUDING:



Claire le paven

Institut d'Electronique et des Télécommun...

77 PUBLICATIONS 248 CITATIONS

SEE PROFILE



Ahmed Ziani

King Abdullah University of Science and Te...

53 PUBLICATIONS 124 CITATIONS

SEE PROFILE



Laurent Le Gendre

Université de Rennes 1

96 PUBLICATIONS 259 CITATIONS

SEE PROFILE

# Photoelectrochemical Properties of Crystalline Perovskite Lanthanum Titanium Oxynitride Films under Visible Light

Claire Le Paven-Thivet,<sup>†</sup> Akio Ishikawa,<sup>‡</sup> Ahmed Ziani,<sup>†</sup> Laurent Le Gendre,<sup>\*,†</sup> Masaaki Yoshida,<sup>‡</sup> Jun Kubota,<sup>‡</sup> Franck Tessier,<sup>§</sup> and Kazunari Domen<sup>‡</sup>

Groupe Antennes et Hyperfréquences, I.E.T.R. UMR-CNRS 6164, Université de Rennes 1, IUT Saint Brieuc, 18 rue Henri Wallon 22004 Saint Brieuc cedex, France, Department of Chemical System Engineering, The University of Tokyo, 7-3-1 Hongo, Bunkyo-ku, Tokyo 113-8650, Japan, and Equipe Verres et Céramiques, Unité Sciences Chimiques de Rennes UMR-CNRS 6226, Université de Rennes 1, Campus de Beaulieu 35042 Rennes cedex, France

Received: December 16, 2008; Revised Manuscript Received: February 13, 2009

Thin films of the lanthanum titanium oxynitride perovskite ( $\text{LaTiO}_x\text{N}_y$ ) synthesized by reactive radio-frequency sputtering on conductive Nb-doped strontium titanate ( $\text{Nb:SrTiO}_3$ ) substrates are evaluated as photoelectrodes for water splitting reaction under visible light. The films are characterized by X-ray diffraction analysis, energy-dispersive spectroscopy, scanning electron and atomic force microscopy, and ultraviolet–visible spectroscopy. Thin films with polycrystalline, oriented, or epitaxial structures are obtained depending on the substrate temperature and plasma composition. The band-gap energies of the films thus prepared are in the range 2.05–2.35 eV. Photoelectrochemical measurements reveal that the photoactivity of these films increases with the quality of film crystallization. The flat-band position of  $\text{LaTiO}_x\text{N}_y$  is found to change with pH of the reactant solution. Surface modification with colloidal  $\text{IrO}_2$  is also demonstrated to result in a marked increase in photoactivity, with the modified epitaxial  $\text{LaTiO}_x\text{N}_y$  film exhibiting a photocurrent density of ca.  $70 \mu\text{A cm}^{-2}$  at +1.0 V vs. Ag/AgCl at pH 4.5 in aqueous  $\text{Na}_2\text{SO}_4$  solution under irradiation at visible wavelengths ( $\lambda > 420 \text{ nm}$ ).

## Introduction

Due to the increasing demand for energy and the growing scarcity of fossil fuels, considerable effort has been devoted to the development of renewable energy in recent years. The use of dihydrogen as an energy carrier, particularly in the automotive sector, could solve a major component of the environmental challenge of this century. This alternative to hydrocarbons becomes feasible as a renewable energy source if the production of dihydrogen itself can be performed by a renewable approach at a realistic cost. Hydrogen production from water splitting using a photocatalyst or photoelectrode has the potential to solve the energy problem by converting solar energy to chemical energy.<sup>1–4</sup> Over the past few decades, many semiconductor materials have been developed for use as photocatalysts or photoelectrodes driven at ultraviolet (UV) wavelengths.<sup>5–8</sup> As the largest proportion of the solar energy spectrum lies in the visible range, more efficient photocatalytic conversion of solar energy could be achieved using a suitable material that is active under visible light. The partial substitution of nitride ions for oxygen in oxide semiconductors has been found to narrow the band gap of the material (1.7–2.5 eV) and thereby extend the photoactivity of the material into the visible range.<sup>1,9,10</sup> Perovskite  $\text{LaTiO}_2\text{N}$ , an example of such a nitride-substituted semiconductor, has been demonstrated to be an effective visible-light-driven photocatalyst for water reduction to  $\text{H}_2$  and water oxidation to  $\text{O}_2$  in the presence of appropriate sacrificial reagents.<sup>11,12</sup>

The preparation of such photoelectrodes as a thin film is a useful approach for the construction of large-scale water splitting systems at relatively low cost, and the preparation of thin films with high crystalline quality is likely to be effective for increasing the process efficiency and the chemical stability of the system. Thin films of quaternary oxynitride perovskites, including  $\text{LaTiO}_x\text{N}_y$ ,<sup>13,14</sup>  $\text{BaTaO}_2\text{N}$ ,<sup>15</sup>  $(\text{La,Sr})\text{Ti}(\text{O,N})_3$ ,<sup>16,17</sup>  $\text{Sr-MoO}_{3-x}\text{N}_x$ ,<sup>18</sup> and  $(\text{Zr,Sn})\text{TiO}_x\text{N}_y$ <sup>19</sup> have been prepared by a range of methods, such as reactive sputtering deposition, pulsed laser deposition, and spin-coating. In the present study,  $\text{LaTiO}_x\text{N}_y$  films are prepared by reactive sputtering under a range of preparation conditions, yielding polycrystalline, oriented, and epitaxial films. The photoelectrochemical properties of these films under irradiation with visible light are then characterized using a range of analytical techniques. The effect of surface modification with colloidal  $\text{IrO}_2$  is also investigated.

## Experimental Methods

$\text{LaTiO}_x\text{N}_y$  films were synthesized by radio-frequency magnetron sputtering at high temperature using a reactive Ar +  $\text{N}_2$  plasma gas. A 3 mm thick sputtering target was formed by cold pressing  $\text{LaTiO}_2\text{N}$  powder, under 80 MPa, into a 40 mm-diameter disk. This oxynitride compound was obtained by nitridation of the corresponding  $\text{La}_2\text{Ti}_2\text{O}_7$  (oxide) powder, which was synthesized by the following molten salt route.  $\text{La}_2\text{O}_3$  and  $\text{TiO}_2$  precursors were mixed in a 1:2 ratio. A salt of composition 50 mol % NaCl/50 mol % KCl was then added, constituting 50 wt % of the total reaction mixture. The corresponding mixture was heated at 1273 K for 15 h. The resulting product was washed several times using distilled water and clearly identified, as  $\text{La}_2\text{Ti}_2\text{O}_7$ , by X-ray diffraction (XRD). No residual KCl or NaCl has been detected. The nitridation reaction was carried

\* Corresponding author. E-mail: laurent.le-gendre@univ-rennes1.fr. Tel: + 33 2 96 60 96 57. Fax: + 33 2 96 60 96 52.

<sup>†</sup> I.E.T.R. UMR-CNRS 6164.

<sup>‡</sup> The University of Tokyo.

<sup>§</sup> UMR-CNRS 6226.

**TABLE 1: Sputtering Conditions and Characteristics of LaTiO<sub>x</sub>N<sub>y</sub> Films**

film	substrate	N <sub>2</sub> plasma content (vol %)	T <sub>S</sub> (K)	thickness (nm)	N/(N + O) ratio	E <sub>g</sub> (eV)	roughness (rms, nm)	crystallization state
LTON-a	Nb:SrTiO <sub>3</sub>	25	1098	1200	0.13	2.30	2.15	epitaxial
	MgO				0.13			
LTON-b	Nb:SrTiO <sub>3</sub>	25	1073	1240	0.14	2.35	3.90	oriented
	MgO				0.14			
LTON-c	Nb:SrTiO <sub>3</sub>	71	1073	1170	0.38	2.05	11.30	polycrystalline
	MgO				0.38			

out by heating the starting material at 1253 K for 15 h under ammonia gas flow (40 L h<sup>-1</sup>) using an electric furnace and alumina boats.<sup>14</sup>

The target, mounted 6 cm from the substrate, was sputtered with an input power of 2.30 W cm<sup>-2</sup>. The chamber was pumped down to a base pressure of 10<sup>-5</sup> Pa, after which the turbomolecular pump was throttled down and the process gas (Ar/N<sub>2</sub>) was blended into the chamber through a leak valve. During deposition, the dynamic pressure was maintained at 1.87 Pa via the leak valve. Depositions were performed at substrate temperatures (T<sub>S</sub>) of 1073 and 1098 K, and the plasma nitrogen content (N<sub>2</sub> plasma vol %) was set at 25% and 71%. In each run, films were deposited on two types of single-crystal substrates obtained from Crystal GmbH (Berlin, Germany). Conductive niobium-doped (0.8 atom %) (001) SrTiO<sub>3</sub> (Nb: SrTiO<sub>3</sub>) was used as substrate for the films concerned by the photoelectrochemical study. The (001) SrTiO<sub>3</sub> substrate has small crystallographic mismatch with the LaTiO<sub>x</sub>N perovskite (ca. 0.86%), promoting an oriented or epitaxial growth of the films. (001) MgO was used as a double, because this transparent substrate allows transmittance and thickness determination.

X-ray diffraction (XRD) patterns were obtained using a Seifert 3003 PTS diffractometer (Cu Kα<sub>1</sub> radiation). Conventional  $\theta$ – $2\theta$  patterns were recorded at 0.01° intervals with a 4 s count time at each step. The crystalline alignment in the plane of the films was investigated through the acquisition of stereo electron channeling patterns (ECP) using a conventional Jeol JSM 6400 scanning electron microscopy (SEM) operating at 25 kV with a working distance of 6 mm. The incident electron beam is rocked by few degrees on the sample, which allows reaching the diffracted Bragg condition for well-aligned planes in epitaxial films. As a result, the backscattered electrons yield profile is considered to be a stereographic projection of the traces of the (*hkl*) planes and can be indexed.<sup>20</sup>

The surface morphology of the films was characterized by atomic force microscopy (AFM) using a Nanoscope III Digital Instrument apparatus in tapping mode and covering a surface area of 5 μm × 5 μm. The error on roughness value is around 0.1 nm.

Cross-sectional observations for thickness measurements were performed using a Jeol JSM 5440 SEM with a tungsten filament operating at 10 kV. The resolution of the SEM images thus obtained is close to 5 nm. Coupled energy-dispersive spectroscopy (EDS) was employed to measure the chemical composition of samples. The N/(N + O) ratios of the present films were obtained as relative values.

UV–visible transmittance spectra were acquired using a Perkin-Elmer Lambda 20 spectrometer in the wavelength range of 200–1100 nm. For each sample, the absorption coefficient  $\alpha$  is calculated from the transmittance (*T*) using the relation  $\alpha = (1/t)(\ln(1/T))$ , where *t* is the thickness of the film.<sup>21</sup> The band gap of the material (E<sub>g</sub>) is calculated assuming a direct allowed transition and using the relation  $(\alpha h\nu)^2 = h\nu - E_g$ , where *hν* is the photon energy. In the plot of  $(\alpha h\nu)^2$  as a function of *hν*,

extrapolation of the linear region of the plot at zero gives the value of E<sub>g</sub>. The error in the value of E<sub>g</sub> thus determined is estimated to be close to 0.05 eV.

Samples for electrochemical characterizations were prepared by attaching a copper wire to the back side of the Nb: SrTiO<sub>3</sub> substrate using silver paste and waterproofing the connection with epoxy resin and polytetrafluoroethylene tape in order to prevent current leakage. Cyclic and linear sweep voltammetry were carried out using a planar-windowed Pyrex photoelectrochemical cell with platinum counter electrode and Ag/AgCl reference electrode (+0.2 V vs normal hydrogen electrode, NHE). The electrochemical cell was filled with 100 cm<sup>3</sup> of an electrolyte consisting of 0.1 M Fe(CN)<sub>6</sub><sup>4-</sup> and 0.1 mM Fe(CN)<sub>6</sub><sup>3-</sup> in aqueous solution, or 0.5 M Na<sub>2</sub>SO<sub>4</sub> in aqueous solution. The electrolyte was saturated with argon prior to electrochemical measurements. The typical photochemical properties were measured under irradiation at visible wavelengths ( $\lambda > 420$  nm) using a xenon lamp (300 W) and UV cutoff filter. The reactant solution was irradiated intermittently by chopping the incident light using an electric shutter operated at 0.25 Hz (opened for 2 s, closed for 2 s). The potential of the electrode was controlled using a potentiostat (HZ-5000, Hokuto Denko).

Colloidal IrO<sub>2</sub> was deposited on the surface of the prepared thin films as a cocatalyst for water oxidation. The colloidal IrO<sub>2</sub> aqueous solution was prepared by hydrolysis of Na<sub>2</sub>IrCl<sub>6</sub>,<sup>22</sup> with the pH of the solution adjusted to 11–12 with NaOH (aq.). The solution was heated in an Erlenmeyer flask at 353 K for 30 min, then cooled to room temperature by immersion in a cold water bath. The pH of the cooled solution was adjusted to 9–10 with HNO<sub>3</sub> (aq). Subsequent heating at 353 K for 30 min resulted in a deep blue solution containing colloidal IrO<sub>2</sub>. The oxynitride films were soaked in an aliquot (10 cm<sup>3</sup>) of the prepared colloidal IrO<sub>2</sub> solution for 30 min, and then washed with distilled water prior to electrochemical measurements.

## Results

The deposition conditions required for obtaining epitaxially grown oxynitride films have been shown to be very specific, involving high substrate temperature and mixed argon and nitrogen atmosphere.<sup>14</sup> The conditions of sputtering deposition in the present study were thus optimized in order to obtain the highest quality films. The deposition parameters and the characteristics of the three films thus prepared are presented in Table 1. In each sputtering run, films were deposited on Nb: SrTiO<sub>3</sub> and MgO substrates. The paired films were confirmed by EDS analysis to be identical with regard to their nitrogen composition and are assumed to be similar in thickness and band-gap value. Films were prepared so as to be approximately 1200 nm thick, as confirmed by SEM cross-section observations (Figure 1).

The EDS chemical compositional analysis reveals that the N/(N + O) ratio in the films is 0.13 for LTON-a, 0.14 for

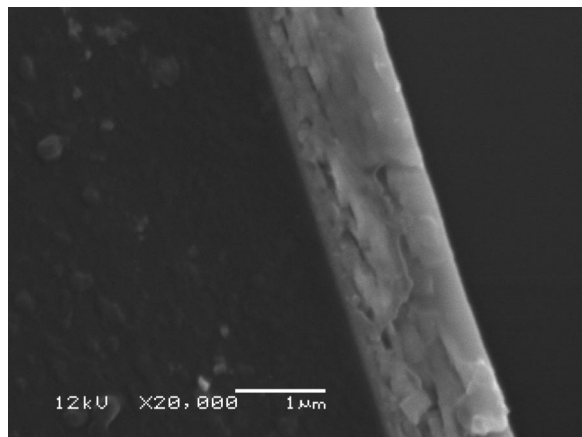


**Figure 1.** SEM cross-section observation of the LTON-a film deposited on MgO substrate.

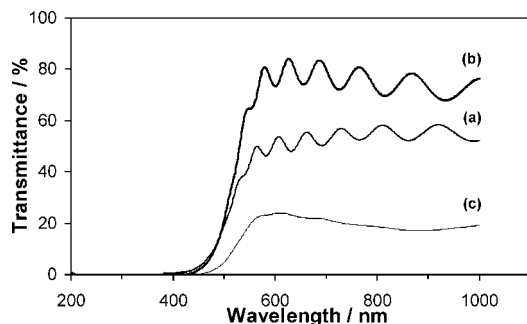


**Figure 2.** UV-visible transmittance spectra for  $\text{LaTiO}_x\text{N}_y$  films deposited on MgO substrates: (a) LTON-a, (b) LTON-b, and (c) LTON-c.

LTON-b and 0.38 for LTON-c (Table 1). All films have a La/Ti atomic ratio close to 1. Due to the limitations of EDS measurement, the lanthanum, titanium, and nitrogen contents can not be determined accurately and simultaneously. The present values need to be taken as relative values for measurements made in the same conditions. Nevertheless, previous wavelength dispersive spectrometry (WDS) measurements made on similar films did support the results found by EDS.<sup>14</sup> So, compared to stoichiometric  $\text{LaTiO}_2\text{N}$  compound, these analysis show that low-nitrogen and high-nitrogen content films can be deposited, depending on the sputtering conditions. This is confirmed by UV-visible transmittance measurements (Figure 2), performed using the films prepared on double-side polished MgO substrates. The films prepared on the two substrates are bright to dark orange in color. As expected, the absorption edge shifts toward longer wavelengths as the  $\text{N}/(\text{N} + \text{O})$  ratio in films increases. The calculated band-gap energy is located in the visible region, ranging from 2.35 to 2.05 eV (Table 1), in good agreement with those determined for other  $\text{LaTiO}_2\text{N}$  materials.<sup>11,16,23–25</sup> This range of band-gap energies is attributable to the range of nitrogen compositions of the films, so that the films are now labelled as  $\text{LaTiO}_x\text{N}_y$ . As the same nitrogen compositions were measured for the paired films, the band-gap energy determined for the films on MgO is considered to be applicable to the corresponding film prepared on Nb:SrTiO<sub>3</sub> under the same conditions.

X-ray diffraction (XRD) measurements by  $\theta$ – $2\theta$  scan were performed for the films deposited on the Nb:SrTiO<sub>3</sub> substrates (Figure 3). Despite the existence of a slight shift to smaller  $2\theta$  angle positions, the LTON-c film pattern is fully consistent with that of  $\text{LaTiO}_2\text{N}$  polycrystalline powder (orthorhombic cell, JCPDS No. 48-1230). The discrepancy of the  $2\theta$  positions from

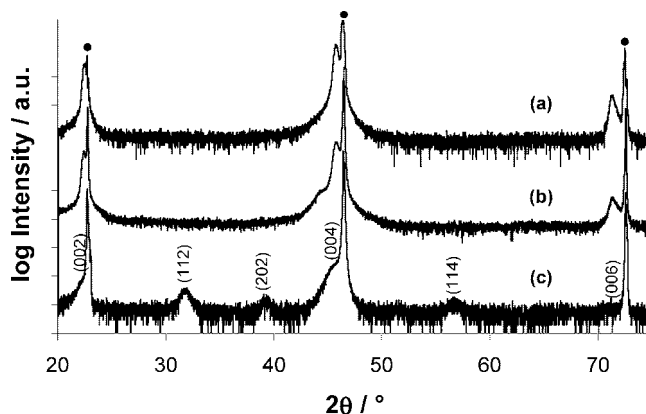


**Figure 3.**  $\theta$ – $2\theta$  XRD patterns for  $\text{LaTiO}_x\text{N}_y$  films deposited on Nb-doped (001) SrTiO<sub>3</sub> substrates: (a) LTON-a, (b) LTON-b, and (c) LTON-c. Peaks labelled as (\*) belong to the (001) Nb:SrTiO<sub>3</sub> substrate.

the ones of  $\text{LaTiO}_2\text{N}$  is due to the non-stoichiometric nitrogen content of the film. Similar deviations are observed for the LTON-a and LTON-b films. The assignment of observed diffracted peaks to the  $\text{LaTiO}_3$  oxide was rejected since this oxide appears to be black in color and is metallic. The presence of the fully oxidized  $\text{LaTiO}_{3.5}$  crystallized compound can not be evidenced in our films. On powder, the intense peaks of this oxide phase are located at angle positions below  $30^\circ$  (for example,  $2\theta_{(-212)} = 29.807^\circ$ , monoclinic cell, JCPDS No. 28-0517). As thin films,  $\text{LaTiO}_{3.5}$  has been deposited as  $(-210)$  oriented films on (001)SrTiO<sub>3</sub><sup>26</sup> and (100) oriented film on (110)SrTiO<sub>3</sub><sup>27</sup>, but the corresponding angle positions ( $2\theta_{(-210)} = 21.131^\circ$ , monoclinic cell, JCPDS No. 28-0517;  $2\theta_{(400)} = 27.698^\circ$ , orthorhombic, JCPDS No. 70-1690) are far from our results. So, the present crystallized oxynitride thin films are identified as  $\text{LaTiO}_x\text{N}_y$  compounds, isostructural to the stoichiometric  $\text{LaTiO}_2\text{N}$  material. Notice that the LTON-b film exhibits a small additional peak at around  $2\theta = 44.500^\circ$  (Figure 3) that could not be assigned to any known phase.

The crystallization state differs among the three films. The LTON-c film is polycrystalline, exhibiting nearly all of the diffraction peaks attributable to the  $\text{LaTiO}_2\text{N}$  parent. The (002) and (004) peaks are stronger than the others, suggesting a weak (001) orientation (based on an orthorhombic cell of  $\text{LaTiO}_x\text{N}_y$ ). The LTON-a and LTON-b films display only (001) peaks, which is characteristic of films with  $c$  axis oriented perpendicular to the film (and substrate) surface. The measured rocking-curves show that the mosaic spread of crystallites around this axis is smaller for the LTON-a film ( $\Delta\theta = 1.01^\circ$ ) than for the LTON-b film ( $\Delta\theta = 4.06^\circ$ ).

The epitaxial growth of the LTON-a film was demonstrated by ECP. When a film is epitaxied, the incident electrons go more and more deeply in the film, in the channels made by the well-ordered crystalline planes perpendicular to the surface. The electrons are backscattered in respect with these specific directions. In this case, the pattern displays an arrow, which can be indexed (not done here). The LTON-a film is the only one exhibiting an arrow (Figure 4a), what reveals that this film is  $c$ -axis oriented, epitaxially grown on the (001) Nb:SrTiO<sub>3</sub> substrate. However, the intermediate value of the rocking curve and the diffuse character of the arrow pattern suggest that the quality of its epitaxy is moderate. When a film is oriented or polycrystalline, the impinging electrons are diffused by the random crystallographic planes perpendicular to the surface and backscattered in all directions: a featureless pattern appears.



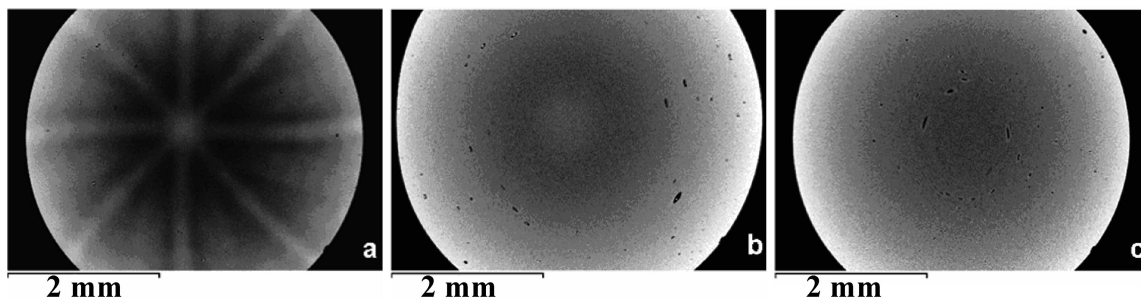


**Figure 4.** ECP results for  $\text{LaTiO}_x\text{N}_y$  films deposited on Nb-doped (001)  $\text{SrTiO}_3$  substrates: (a) LTON-a, (b) LTON-b, and (c) LTON-c.

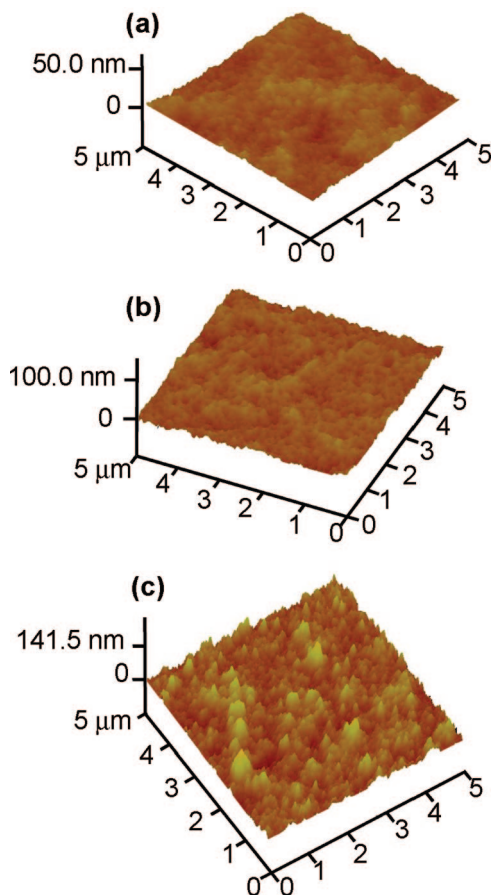


**Figure 5.** AFM images showing surface morphologies for  $\text{LaTiO}_x\text{N}_y$  films deposited on Nb-doped (001)  $\text{SrTiO}_3$  substrates: (a) LTON-a, (b) LTON-b, and (c) LTON-c films.

This is the case for the oriented LTON-b film (Figure 4b) and polycrystalline LTON-c film (Figure 4c).

It is well known that the roughness of a film increases with its thickness.<sup>28</sup> As the present films are of similar thicknesses, the roughnesses of the films can be validly compared. As indicated in Table 1 and shown in Figure 5, the surface morphologies of the films deposited on the Nb: $\text{SrTiO}_3$  substrates are related to the quality of their crystalline growth. The crystalline epitaxially grown film (LTON-a) exhibits the lowest root-mean-square (rms) roughness (2.2 nm), whereas the oriented film (LTON-b) has an rms roughness of 3.9 nm. The polycrystalline film (LTON-c) has an rms roughness of 11.3 nm, consistent with granular composition of the surface.

The photoelectrochemical properties of the prepared films were evaluated through the measurement of current-potential in a solution containing 0.1 mM  $\text{Fe}(\text{CN})_6^{3-}$  and 0.1 M  $\text{Fe}(\text{CN})_6^{4-}$  under intermittent irradiation with visible light ( $\lambda > 420$  nm).

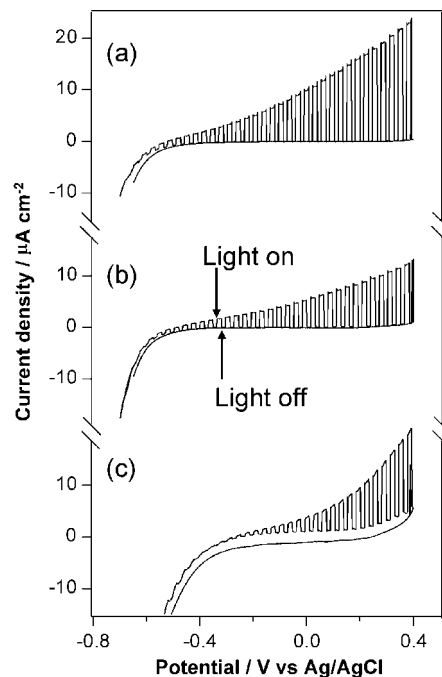


**Figure 6.** Current-potential curves for (a) LTON-a, (b) LTON-b, and (c) LTON-c films in 0.1 M  $\text{Fe}(\text{CN})_6^{4-}$  and 0.1 M  $\text{Fe}(\text{CN})_6^{3-}$  under intermittent irradiation with UV and visible light ( $\lambda > 420$  nm) at a scan rate of 10 mV/s (pH 7.8).

Figure 6 shows the current-potential curves measured in the range  $-0.8$  to  $+0.4$  V vs Ag/AgCl at a scan rate of  $10 \text{ mV s}^{-1}$ . Anodic photocurrent was observed for all films, indicative of the oxidation of  $\text{Fe}(\text{CN})_6^{4-}$ . No response was observed for the bare Nb: $\text{SrTiO}_3$  substrate (an n-type semiconductor) under visible light, as expected from the wide band gap of the material (3.0 eV). The present results thus demonstrate that the thin films prepared in this study function as n-type semiconductor electrodes under visible light. The LTON-a film exhibits the highest anodic current density of the present films and was thus employed for all subsequent electrochemical measurements.

The current-potential curve for the LTON-a electrode in aqueous 0.5 M  $\text{Na}_2\text{SO}_4$  solution under intermittent irradiation with visible light (Figure 7) shows that anodic photocurrent was also generated under these conditions. In aqueous  $\text{Na}_2\text{SO}_4$  solution, the water and/or the thin film would be oxidized by holes generated in the valence band of  $\text{LaTiO}_x\text{N}_y$  at more positive potential than the flat-band potential ( $E_{\text{FB}}$ ). As  $\text{LaTiO}_2\text{N}$  powder is known to exhibit stable photocatalytic activity for water oxidation to  $\text{O}_2$  in aqueous solution containing  $\text{AgNO}_3$ ,<sup>11</sup> the present observation of anodic photocurrent is attributable to the water oxidation reaction.

The efficiency of the water oxidation reaction using a  $\text{LaTiO}_2\text{N}$  powder suspension has been shown in previous work

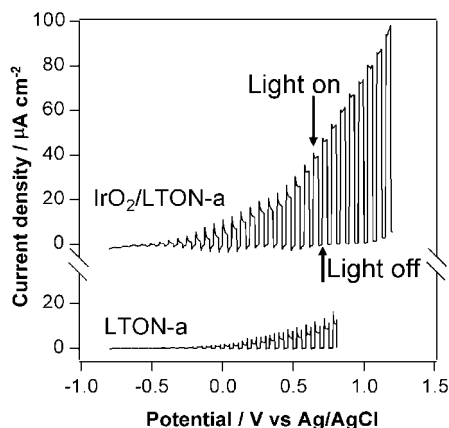


**Figure 7.** Current–potential curves for LTON-a and IrO<sub>2</sub>/LTON-a films under intermittent irradiation with visible light ( $\lambda > 420$  nm) in 0.5 M Na<sub>2</sub>SO<sub>4</sub> (pH 4.5).

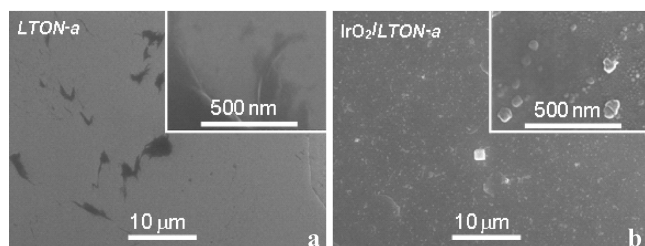


**Figure 8.** SEM images for (a) LTON-a and (b) IrO<sub>2</sub>/LTON-a films.

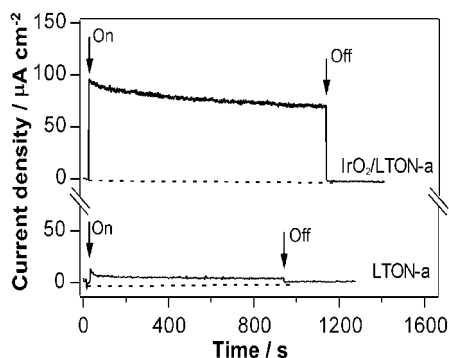


**Figure 9.** Current–time evolution for LTON-a and IrO<sub>2</sub>/LTON-a films in aqueous 0.5 M Na<sub>2</sub>SO<sub>4</sub> solution at +1.0 V vs Ag/AgCl under visible irradiation.

to be improved by modification of the photocatalytic powder with colloidal IrO<sub>2</sub>.<sup>11</sup> Modification of the present LaTiO<sub>x</sub>N<sub>y</sub> films with colloidal IrO<sub>2</sub> was thus examined as part of the present study. SEM images of the films before and after loading with colloidal IrO<sub>2</sub> are shown in Fig. 8. These images confirm that the colloidal IrO<sub>2</sub> was dispersed on the film as agglomerates of up to 200 nm in diameter. The current–potential curves before and after IrO<sub>2</sub> loading are shown in Figure 7. The photocurrent density on the IrO<sub>2</sub>/LTON-a film is approximately 5 times higher than on the unmodified LTON-a at +0.8 V vs Ag/AgCl. This increase in anodic photocurrent was also observed for the other films prepared in this study upon modification with IrO<sub>2</sub>.

Figure 9 shows current curves for the LTON-a and IrO<sub>2</sub>/LTON-a films at +1.0 V vs Ag/AgCl under irradiation with visible light. The anodic photocurrent can be seen to decrease gradually over time, attributable to surface oxidation of the LaTiO<sub>x</sub>N<sub>y</sub> film and/or dissolution of the IrO<sub>2</sub> particles off the surface. Under these conditions, IrO<sub>2</sub> loading results in a

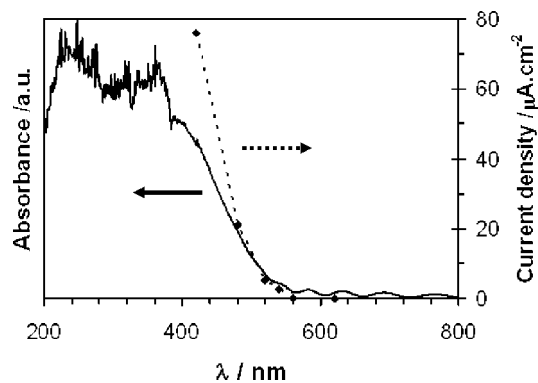


**Figure 10.** Dependence of photocurrent density for IrO<sub>2</sub>/LTON-a film at +1.0 V vs Ag/AgCl on wavelength of incident light (0.5 M Na<sub>2</sub>SO<sub>4</sub>, pH 4.5), and absorbance spectrum of LTON-a film deposited on MgO substrate.

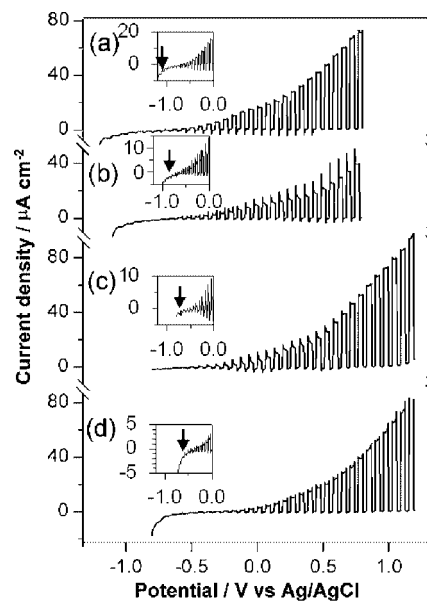


**Figure 11.** Current–potential curves for IrO<sub>2</sub>/LTON-a film in aqueous 0.5 M Na<sub>2</sub>SO<sub>4</sub> solution under intermittent irradiation with visible light ( $\lambda > 420$  nm) at pH of (a) 11.4, (b) 9.2, (c) 6.9, and (d) 4.4 (scan rate, 10 mV/s). Onset potential position is marked by an arrow in the insert.

photocurrent density approximately 16 times higher than that for the unmodified film.

Figure 10 shows the dependence of anodic photocurrent density on the cutoff wavelength of incident light for the IrO<sub>2</sub>/LTON-a film. Photocurrent was observed at wavelengths of up to 540 nm, in very good agreement with the absorbance spectrum of the paired film deposited on MgO substrate. The photooxidation reaction can therefore be confirmed to proceed via the band-gap transition of LaTiO<sub>x</sub>N<sub>y</sub>.

The flat-band potentials were determined as a function of pH from photocurrent measurements of the IrO<sub>2</sub>-loaded film. Figure 11 shows the current–potential curves measured in solutions with pH of 4.4–11.4. Anodic photocurrent was observed in all solutions. The onset potential, corresponding to the flat-band potential, was shifted negatively with increasing pH. The energy difference between the conduction band edge potential ( $E_{CB}$ ) and  $E_{FB}$  is assumed to be ca. 0.1 eV considering the insulating n-type semiconducting character of LaTiO<sub>x</sub>N<sub>y</sub>.<sup>29</sup> Using the LaTiO<sub>x</sub>N<sub>y</sub> band gap of 2.1 eV,<sup>11</sup> the valence band edge potential ( $E_{VB}$ ) is estimated to be 2.1 V more positive than  $E_{CB}$ . Figure 12 shows the conduction and valence band edge potentials of

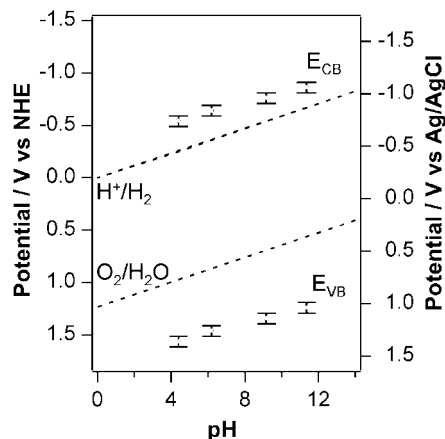


**Figure 12.** Dependence of conduction and valence band edge potentials for  $\text{LaTiO}_x\text{N}_y$  film on pH of electrolyte as determined from photocurrent measurements.

the  $\text{LaTiO}_x\text{N}_y$  film as a function of pH. The top and lower band-gap positions of  $\text{LaTiO}_x\text{N}_y$  are therefore dependent on pH, with a change of approximately  $-60$  mV/pH. The established band-gap positions of  $\text{LaTiO}_x\text{N}_y$  are satisfactory for oxidizing water at all pH against the counter electrode evolution of  $\text{H}_2$ , consistent with the results of photocatalytic reactions. These results demonstrate that  $\text{LaTiO}_x\text{N}_y$  can be used to drive photoelectrochemical reactions for water splitting.

## Discussion

The use of a thin film catalyst instead of a powder catalyst will make it possible, from a technical point of view, to produce very large reaction surfaces with only a small amount of  $\text{LaTiO}_x\text{N}_y$  material. The performance of the powder form in photocatalytic reactions without a cocatalyst is known to be determined by the combination of several parameters, such as composition, crystallization quality, morphology, and defect density.<sup>30</sup> For sputtered films, the composition and crystallographic structure (including defects) are the dominant parameters affecting performance.<sup>31,32</sup> As the range of surface roughness variation among sputtered films is here relatively small, the influence of surface roughness of thin films on their photocatalytic performance is considered to be much weaker than the effect of specific surface area for powder materials.

The composition and crystallization state of the  $\text{LaTiO}_x\text{N}_y$  film are interdependent, as noted previously.<sup>14</sup> Here, the films with higher nitrogen content are polycrystalline, while those with lower nitrogen content are epitaxially grown. Although the visible absorption edge of the nitrogen-rich films is located at wavelengths more suitable for the utilization of visible light, these films exhibit lower photon-to-current conversion efficiency than the low-nitrogen compositions. As previously noticed on visible light-driven photocatalytic activity of  $\text{LaTi}(\text{O},\text{N})_3$  nano-particles,<sup>25</sup> there is thus a trade-off between the optimization of active wavelength and structure-related conversion efficiency. From the homologous series developed for perovskite-related layered oxide materials,<sup>33</sup>  $\text{LaTiO}_x\text{N}_y$  compounds could be described using a generic formula  $\text{La}_n\text{Ti}_n(\text{O},\text{N})_{3n+2}$ . This notation puts into relief a structure resulting from the stacking of  $n$ -size perovskite blocks (containing  $\text{Ti}(\text{O},\text{N})_6$  units) separated by interlayer spaces. That way, lanthanum titanium oxynitrides thin films could be understood as a mixture of diverse-sized perovskite blocks irregularly distributed from  $\text{La}_4\text{Ti}_4\text{O}_{14}$  ( $n = 4$ ) to  $\text{LaTiO}_2\text{N}$  ( $n = \infty$ ). An important nitrogen/oxygen substitution into the parent oxide structure leads to an increase of the

average  $n$  value as well as the loss of the layering periodicity what could lead to an XRD pattern only containing  $\text{LaTiO}_2\text{N}$  contribution.<sup>25</sup> Our results on thin films support this assumption since no crystallized  $\text{LaTiO}_{3.5}$  material has been detected in XRD patterns and no shoulder has been observed in UV–visible transmittance curves.

Depending on the deposition conditions, the nitrogen film content will control the band-gap value (electronic structure of the  $\text{Ti}(\text{O},\text{N})_6$  octaetra) as well as the amount of the interlayers spaces that act as physical separation sites where electron-hole recombination is retarded.<sup>34</sup> As observed on oxynitride  $\text{LaTi}(\text{O},\text{N})_3$  nano-particles<sup>25</sup> and N-doped  $\text{Sr}_2\text{Nb}_2\text{O}_7$  powders,<sup>35</sup> the photocatalytic efficiency of the oxynitride materials is limited, for the weakly nitrated materials, by their visible light absorption ability, and for the N-rich compounds, by the decrease of the interlayer spaces density. In the two cases, the quality of the crystallization is also of great importance since it influences the number of defects, sites for electron-hole recombination.

The photoresponse of the present films clearly increases in the sequence  $\text{LTON-c} < \text{LTON-b} < \text{LTON-a}$ , indicating that the positive effects of low nitrogen content and film structure are dominant over its visible light absorption capacity (band-gap value). High-quality crystallization in oriented oxynitride films is also likely to inhibit the formation of defects associated with grain boundaries, substrate mismatch and oxygen vacancies, which can act as centers for the recombination of photogenerated electrons and holes. The superior photoresponse of the epitaxially-grown film confirms that well-aligned perovskite layers promote the effective space separation of photoreactions.<sup>36</sup>

## Conclusions

Thin  $\text{LaTiO}_x\text{N}_y$  films deposited by reactive radio frequency magnetron sputtering on single-crystalline Nb-doped  $\text{SrTiO}_3$  substrates under a range of conditions were found to develop dissimilar crystalline states. Three films, with polycrystalline, oriented, or epitaxial structures, were thus obtained. Through measurement of current-potential curves in  $[\text{Fe}(\text{CN})_6]^{3-}/[\text{Fe}(\text{CN})_6]^{4-}$  and  $\text{Na}_2\text{SO}_4$  aqueous solutions under irradiation with visible light, it was demonstrated that these oxynitride films function as  $n$ -type semiconductor electrodes with band gaps of 2.05–2.35 eV. Modification of the films by deposition of colloidal  $\text{IrO}_2$  was found to significantly enhance the photocurrent associated with the water oxidation reaction. The  $\text{IrO}_2$ -loaded epitaxial  $\text{LaTiO}_x\text{N}_y$  film exhibited the highest photocurrent density of the present films, ca.  $70 \mu\text{A cm}^{-2}$  at +1.0 V vs Ag/AgCl and pH 4.5 in aqueous  $\text{Na}_2\text{SO}_4$  solution under irradiation with visible light. The band-gap positions of all of the  $\text{LaTiO}_x\text{N}_y$  films were found to be suitable for the oxidation and reduction of water over a wide range of pH (4–12). The results suggest that the improved crystallinity achieved by the epitaxial growth, as well as the low-nitrogen content, may be responsible of the higher photoreactivity of this film. Thin films of the oxynitride perovskite  $\text{LaTiO}_x\text{N}_y$  have thus been demonstrated to drive photoelectrochemical reactions for water splitting under irradiation with visible light.

**Acknowledgment.** This work was supported by the Research and Development in a New Interdisciplinary Field Based on Nanotechnology and Materials Science program of the Ministry of Education, Culture, Sports, Science and Technology (MEXT) of Japan. Acknowledgement is also extended to the Global Center of Excellence (GCOE) Program for Chemistry Innovation. The authors acknowledge S. Casale and R. Tartivel of the

University of Rennes 1 for ECP and AFM measurements, respectively, and M. Philippon for valuable discussions.

## References and Notes

- (1) Kudo, A.; Kato, H.; Tsuji, I. *Chem. Lett.* **2004**, 33, 1534.
- (2) Maeda, K.; Domen, K. *J. Phys. Chem. C* **2007**, 111, 7851.
- (3) Hoertz, P. G.; Mallouk, T. E. *Inorg. Chem.* **2005**, 44, 6828.
- (4) Lee, J. S. *Catal. Surv. Asia* **2005**, 9, 217.
- (5) Fujishima, A.; Honda, K. *Nature* **1972**, 238, 37.
- (6) Domen, K.; Naito, S.; Soma, M.; Onishi, T.; Tamaru, K. *J. Chem. Soc., Chem. Commun.* **1980**, 543.
- (7) Darwent, J. R.; Mills, A. *J. Chem. Soc., Faraday Trans. II* **1982**, 78, 359.
- (8) Osterloh, F. E. *Chem. Mater.* **2008**, 20, 35.
- (9) Asahi, R.; Morikawa, T.; Ohwaki, T.; Aoki, K.; Taga, Y. *Science* **2001**, 293, 269.
- (10) Maeda, K.; Teramura, K.; Lu, D.; Takata, T.; Saito, N.; Inoue, Y.; Domen, K. *Nature* **2006**, 440, 295.
- (11) Kasahara, A.; Nukumizu, K.; Hitoki, G.; Takata, T.; Kondo, J. N.; Hara, M.; Kobayashi, H.; Domen, K. *J. Phys. Chem. A* **2002**, 106, 6750.
- (12) Kasahara, A.; Nukumizu, K.; Takata, T.; Kondo, J. N.; Hara, M.; Kobayashi, H.; Domen, K. *J. Phys. Chem. B* **2003**, 107, 791.
- (13) Le Gendre, L.; Le Paven, C.; Pinel, J.; Fasquelle, D.; Carru, J. C.; Cheviré, F.; Tessier, F.; Marchand, R. *Silicates Industriels* **2004**, 69, 165.
- (14) Le Paven-Thivet, C.; Le Gendre, L.; Le Castrec, J.; Cheviré, F.; Tessier, F.; Pinel, J. *Progr. Solid State Chem.* **2007**, 35, 299.
- (15) Kim, Y.-I.; Si, W.; Woodward, P. M.; Sutter, E.; Park, S.; Vogt, T. *Chem. Mater.* **2007**, 19, 618.
- (16) Aguiar, R.; Weidenkaff, A.; Schneider, C.W.; Reller, A.; Ebbinghaus, G. *Progr. Solid State Chem.* **2007**, 35, 291.
- (17) Aguiar, R.; Logvinovich, D.; Weidenkaff, A.; Karl, H.; Schneider, C. W.; Reller, A.; Ebbinghaus, S. G. *Mat. Res. Bull.* **2008**, 43, 1376.
- (18) Lekshmi, I. C.; Gayen, A.; Hedge, M. S. *Mat. Res. Bull.* **2005**, 40, 93.
- (19) Lu, X. B.; Liu, Z. G. *J. Elec. Mat.* **2001**, 30, 554.
- (20) Perrin, A.; Guilloux-Viry, M.; Le Paven-Thivet, C.; Jegaden, J.C.; Sergent, M.; Le Lannic, J. *Jeol News* **1992**, 2, 26.
- (21) Kim, S. S.; Choi, S. Y.; Park, C. G.; Jin, H. W. *Thin Solid Films* **1999**, 347, 155.
- (22) Ishikawa, A.; Takata, T.; Kondo, J. N.; Hara, M.; Kobayashi, H.; Domen, K. *J. Am. Chem. Soc.* **2002**, 124, 13547.
- (23) Cheviré, F.; Tessier, F.; Marchand, R. *Eur. J. Inorg. Chem.* **2006**, 6, 1223.
- (24) Ebbinghaus, S. G.; Aguiar, R.; Weidenkaff, A.; Gsell, S.; Reller, A. *Solid State Sci.* **2008**, 10, 709.
- (25) Aguiar, R.; Kalytta, A.; Reller, A.; Weidenkaff, A.; Ebbinghaus, S. G. *J. Mater. Chem.* **2008**, 18, 4260.
- (26) Ohtomo, A.; Muller, D. A.; Grazul, J. L.; Hwang, H. Y. *Appl. Phys. Lett.* **2002**, 80, 3922.
- (27) Fompeyrine, J.; Seo, J. W.; Locquet, J. P. *J. Eur. Ceram. Soc.* **1999**, 19, 1493.
- (28) Thornton, J. A. *J. Vac. Sci. Technol.* **1977**, 11, 666.
- (29) Matsumoto, Y. *J. Solid State Chem.*, 126, 227.
- (30) Li, D.; Hung, H.; Chen, X.; Chen, Z.; Li, W.; Ye, D.; Fu, X. *J. Solid State Chem.* **2007**, 180, 2630.
- (31) Xiao, W.; Yuan, J.; Zhang, Y.; Shangguan, W. *Mat. Chem. Phys.* **2007**, 105, 6.
- (32) Prabakar, K.; Takahashi, T.; Nezuka, T.; Takahashi, K.; Nashima, T.; Kubota, Y.; Fujishima, A. *Renewable Energy* **2008**, 33, 277.
- (33) Lichtenberg, F.; Herrnberger, A.; Wideenmann, K.; Mannhart, J. *Progr. Solid State Chem.* **2001**, 29, 1.
- (34) Kim, J.; Hwang, D. W.; Bae, S. W.; Kim, Y. G.; Lee, J. S. *Kor. J. Chem. Eng.* **2001**, 18, 941.
- (35) Ji, S. M.; Borse, P. H.; Kim, H. G.; Hwang, D. W.; Jang, J. S.; Bae, S. W.; Lee, J. S. *Phys. Chem. Chem. Phys.* **2005**, 7, 1315.
- (36) Domen, K.; Kudo, A.; Shinozaki, A.; Tanaka, A.; Maruya, K.; Onishi, T. *J. Chem. Soc., Chem. Comm.* **1986**, 356.

JP811100R